

AGILE Observations of Two Repeating Fast Radio Bursts with Low Intrinsic Dispersion Measures

C. CASENTINI,^{1,2} F. VERRECCHIA,^{3,4} M. TAVANI,^{1,5} A. URSI,¹ L.A. ANTONELLI,⁴ A. ARGAN,¹ G. BARBIELLINI,⁶
A. BULGARELLI,⁷ P. CARAVEO,^{8,9} M. CARDILLO,¹ P.W. CATTANEO,⁹ A. CHEN,¹⁰ E. COSTA,¹ I. DONNARUMMA,¹¹
M. FEROCI,¹ A. FERRARI,¹² F. FUSCHINO,⁷ M. GALLI,^{7,13} A. GIULIANI,⁸ C. LABANTI,⁷ F. LAZZAROTTO,¹⁴ P. LIPARI,^{15,16}
F. LONGO,⁶ F. LUCARELLI,^{3,4} M. MARISALDI,¹⁷ A. MORSELLI,² F. PAOLETTI,^{18,1} N. PARMIGGIANI,⁷ A. PELLIZZONI,¹⁹
G. PIANO,¹ M. PILIA,¹⁹ C. PITTORI,^{3,4} AND S. VERCELLONE²⁰

¹INAF/IAPS, via del Fosso del Cavaliere 100, I-00133 Roma (RM), Italy

²INFN Sezione di Roma 2, via della Ricerca Scientifica 1, I-00133 Roma (RM), Italy

³SSDC/ASI, via del Politecnico snc, I-00133 Roma (RM), Italy

⁴INAF – Osservatorio Astronomico di Roma, via Frascati 33, I-00078 Monte Porzio Catone (RM), Italy

⁵Università degli Studi di Roma Tor Vergata, via della Ricerca Scientifica 1, I-00133 Roma (RM), Italy

⁶Dipartimento di Fisica, Università di Trieste and INFN, via Valerio 2, I-34127 Trieste (TR), Italy

⁷INAF/OAS, via Gobetti 101, I-40129 Bologna (BO), Italy

⁸INAF/IASF, via E. Bassini 15, I-20133 Milano (MI), Italy

⁹INFN Sezione di Pavia, via U. Bassi 6, I-27100 Pavia (PV), Italy

¹⁰School of Physics, Wits University, Johannesburg, South Africa

¹¹ASI, via del Politecnico snc, I-00133 Roma (RM), Italy

¹²CIFS presso Dipartimento di Fisica, Università di Torino, via P. Giuria 1, I-10125, Torino, Italy

¹³ENEA Bologna, via don Fiammelli 2, I-40128 Bologna (BO), Italy

¹⁴INAF – Osservatorio Astronomico di Padova, vicolo Osservatorio 5, I-35122 Padova (PD), Italy

¹⁵Dipartimento Fisica, Università La Sapienza, p.le Aldo Moro 2, I-00185 Roma (RM), Italy

¹⁶INFN Sezione di Roma 1, p.le Aldo Moro 2, I-00185 Roma, Italy

¹⁷Birkeland Centre for Space Science, Department of Physics and Technology, University of Bergen, Norway

¹⁸East Windsor RSD, 25A Leshin Lane, Hightstown, NJ-08520, USA

¹⁹INAF – Osservatorio Astronomico di Cagliari, via della Scienza 5, I-09047 Selargius (CA), Italy

²⁰INAF – Osservatorio Astronomico di Brera, via E. Bianchi 46, I-23807 Merate (LC), Italy

ABSTRACT

We focus on two repeating fast radio bursts (FRBs) recently detected by the CHIME/FRB experiment in 2018–2019 (Source 1: 180916.J0158+65, and Source 2: 181030.J1054+73). These sources have low excess dispersion measures (DMs) ($< 100 \text{ pc cm}^{-3}$ and $< 20 \text{ pc cm}^{-3}$, respectively), implying relatively small maximal distances. They were repeatedly observed by *AGILE* in the MeV–GeV energy range. We do not detect prompt emission simultaneously with these repeating events. This search is particularly significant for the submillisecond and millisecond integrations obtainable by *AGILE*. The sources are constrained to emit a MeV-fluence in the millisecond range below $F'_{\text{MeV}} = 10^{-8} \text{ erg cm}^{-2}$ corresponding to an isotropic energy near $E_{\text{MeV},UL} \simeq 2 \times 10^{46} \text{ erg}$ for a distance of 150 Mpc (applicable to Source 1). We also searched for γ -ray emission for time intervals up to 100 days, obtaining 3σ upper limits (ULs) for the average isotropic luminosity above 50 MeV, $L_{\gamma,UL} \simeq (5\text{--}10) \times 10^{43} \text{ erg s}^{-1}$. For a source distance near 100 kpc (possibly applicable to Source 2), our ULs imply $E_{\text{MeV},UL} \simeq 10^{40} \text{ erg}$, and $L_{\gamma,UL} \simeq 2 \times 10^{37} \text{ erg s}^{-1}$. Our results are significant in constraining the high-energy emission of underlying sources such as magnetars, or other phenomena related to extragalactic compact objects,

claudio.casentini@inaf.it

francesco.verrecchia@inaf.it

marco.tavani@inaf.it

and show the prompt emission to be lower than the peak of the 2004 magnetar outburst of SGR 1806-20 for source distances less than about 100 Mpc.

1. INTRODUCTION

Fast radio bursts (FRBs) are a new transient phenomenon of unknown origin consisting of bright millisecond radio pulses (mainly at ~ 1 GHz) having large dispersion measures (DMs) in excess of Galactic values (Lorimer et al. 2007; Cordes & Chatterjee 2019). For most of the sources with isotropic sky distribution, a single radio burst has been detected. A smaller number of FRBs show repeating pulses that appear to occur erratically in time (see the FRB catalog, FRBCAT¹; Petroff et al. 2016). No clear evidence for physically different populations has been obtained.

The possible cosmological origin of a sample of FRBs was confirmed at least for one source, the first repeater FRB 121102 (Spitler et al. 2016), which was localized in a dwarf galaxy at $z = 0.193$ ($DM = 560 \text{ pc cm}^{-3}$) with a persistent radio emission (Chatterjee et al. 2017; Marcote et al. 2017). Various models have been proposed to explain the FRB radio emission which is characterized by a few-milliseconds timescale and microsecond sub-burst structure (Champion et al. 2016; Michilli et al. 2018; Hessels et al. 2019). Possible underlying sources include compact objects such as supermassive black holes or young magnetars in young or relatively aged remnants (Metzger et al. 2019). The enigmatic nature of FRBs results from the milliseconds timescale emission and detected fluences implying energies of radio emission near 10^{39} erg for sources at extragalactic distances. Such large energies and implied radio luminosities suggest a physical production mechanism with no analog found in known Galactic sources.

Recently, the CHIME/FRB collaboration has reported the discovery of an additional repeating FRB, FRB 180814.J0453 (CHIME/FRB Collaboration et al. 2019a,b), and later of eight new repeating sources (CHIME/FRB Collaboration et al. 2019c, hereafter C19) with DM ranging from 103.5 to 1281 pc cm^{-3} . The characteristics of this latter sample of repeating FRBs are particularly interesting for counterpart searches, as we elaborate below. High-energy counterpart searches for FRBs different from those of C19 have been recently reported (Scholz et al. 2017; Cunningham et al. 2019; Martone et al. 2019; Marcote et al. 2020).

AGILE is a space mission of the Italian Space Agency (ASI) devoted to X-ray and γ -ray astrophysics (Tavani et al. 2009), operating since 2007 in an equatorial orbit. Due to its spinning operational mode, every 7 minutes

it exposes $\sim 80\%$ of the entire sky. The instrument consists of four different detectors: an imaging γ -ray Silicon Tracker (sensitive in the energy range 30 MeV – 30 GeV; Barbiellini et al. 2002), an X-ray imager, Super-*AGILE* (Super-A, operating in the energy range 20 – 60 keV; Feroci et al. 2007), the mini-calorimeter (MCAL, sensitive in the range 0.35 – 100 MeV; Marisaldi et al. 2008; Fuschino et al. 2008; Labanti et al. 2009) with 4π acceptance, and the anticoincidence (AC) system (Tavani et al. 2009). The combination of the Tracker, MCAL, and the AC working together constitutes the γ -ray imager (GRID) capable of detecting γ -ray transients and gamma-ray burst (GRB)-like phenomena with a good sensitivity. The GRID has a field of view (FoV) with a radius of 70° around pointing direction, while Super-A has a 2D-coded FoV region of radius $\sim 32^\circ$. The MCAL detector is equipped with a special triggering system capable of detecting MeV transients (e.g., gamma-ray bursts, GRBs) on timescales ranging from submilliseconds to hundreds of seconds.

AGILE data are transmitted to the ground at the ASI Malindi (Kenya) ground station, and delivered to the *AGILE* Data Center (ADC; part of the ASI Space Science Data Center). Scientific data are then processed by a fast dedicated pipeline which was recently enhanced for the search of electromagnetic counterparts of gravitational wave sources (Verrecchia et al. 2018; Ursi et al. 2019; Verrecchia et al. 2019). *AGILE* data processing can typically produce alerts for transient γ -ray sources and/or GRB-like events within 20 minutes to 2 hr from satellite onboard acquisition depending on orbital and satellite parameters (Pittori et al. 2013; Bulgarelli et al. 2014).

We report in this paper high-energy observations by *AGILE* of two repeating FRBs recently reported by CHIME (C19) which are characterized by low intrinsic DMs (among the smallest ever determined).

2. TWO REPEATING FRBS WITH LOW INTRINSIC DM

Among the sample of the eight repeating FRBs of C19, two have quite low DMs in excess of their respective Galactic disk and halo contributions: FRB180916.J0158+65 (Source 1), and FRB181030.J1054+73 (Source 2). Table 1 summarizes the characteristics of these repeating radio burst sources, providing the time and the measured radio fluences on millisecond timescales.

Source 1 is of particular interest because it emitted 10 bursts within a 6 month timescale with an average

¹ <http://www.frbcat.org/>

DM $\sim 349 \text{ pc cm}^{-3}$. Its position is near the Galactic plane at coordinates $l = 129.7^\circ$, $b = 3.7^\circ$, within an uncertainty region of 0.09 square degrees. The range of possible Galactic contributions to the dispersion measure, DM_{gal} , according to two different models (Cordes & Lazio 2002; Yao et al. 2017) is between 200 and 325 pc cm^{-3} (C19). Taking into account the Galactic halo contribution to the DM (estimated to be in the range $\text{DM}_{halo} \simeq 50 - 80 \text{ pc cm}^{-3}$; Prochaska & Zheng 2019) the residual excess DM is therefore be quite low ($\lesssim 100 \text{ pc cm}^{-3}$). The conclusion of C19 was that if Source 1 is extragalactic, it is in any case one of the nearest repeating FRBs. Assuming the intergalactic (IGM)-DM relation $DM \simeq 900 z \text{ pc cm}^{-3}$ (McQuinn 2014), we obtain the maximum redshift $z_{max} \sim 0.1$ for a maximum excess DM of 100 pc cm^{-3} (C19). These considerations have been confirmed by the recent millisecond positioning of Source 1 that appears to be associated with a nearby galaxy at the distance of about 150 Mpc (Marquette et al. 2020).

Source 2, located within an uncertainty region of 0.24 square degrees with centroid Galactic coordinates $l = 1,133.4^\circ$, $b = 40.9^\circ$, has the lowest overall DM value ever determined for an FRB ($\text{DM} = 103.5 \text{ pc cm}^{-3}$). The range of DM_{gal} for different models is between 32 and 40 pc cm^{-3} (C19). Taking into account the Galactic halo contribution $\text{DM}_{halo} \simeq 50 - 80 \text{ pc cm}^{-3}$ (Prochaska & Zheng 2019), the excess DM is near 20 pc cm^{-3} or less; the inferred redshift is therefore $z < 0.023$, which implies a maximum luminosity distance less than 100 Mpc.

3. AGILE OBSERVATIONS

We searched in the recent *AGILE* archival data for possible exposures of the location regions of Source 1 and Source 2. *AGILE* is operating in spinning mode since 2009 with a revolution of its axis around the Sun-satellite direction every 7 minutes. This mode allows the *AGILE*/GRID to cover 80% of the sky more than 100 times a day. Gamma-ray exposures of any accessible field last ~ 2 minutes for every satellite revolution with a typical flux sensitivity $\sim 10^{-8} \text{ erg cm}^{-2} \text{ s}^{-1}$ above 30 MeV. Furthermore, *AGILE* is the only mission equipped with the onboard submillisecond triggering capability of *AGILE*/MCAL. This makes possible the detection of very fast events in the range 0.4–100 MeV (such as Terrestrial Gamma-ray Flashes detected in the submillisecond range; Tavani et al. 2011; Marisaldi et al. 2014).

Based on the FRB data of Table 1, we first verified the *AGILE* coverage at the times of the FRB occurrences. Depending on data availability, Earth occultation, and detector operations, we first determine for all interest-

ing cases the proper exposure of the *AGILE* detectors (MCAL, GRID and Super-A) at the radio burst times (T_0). It is possible that at T_0 the event location is either occulted by the Earth, or it is inside the sky exclusion region in the solar/antisolar directions. We mark such cases with "NO" in Table 1. We mark with "YES" cases for which the radio event is accessible by the *AGILE* detectors.

As reported in Table 1, MCAL had exposure for eight bursts of Source 1; two of them were also in the GRID FoV, and none were in the Super-A one. Figure 1 (right panels) shows the positions of two events (F and G of Table 1) of Source 1 and the simultaneous FoV of the GRID and Super-A at their respective T_0 .

In these plots the FRB positions are marked by red stars, the blue line represents the edge of the GRID FoV, the purple circle the edge of Super-A FoV. Every event that falls between the center of the purple circle and the blue line is accessible by the GRID. In the left panels of Figure 1 we show the GRID and Super-A FoVs at $T_0 - 100$ s for which the satellite had a better coverage of source position.

Regarding Source 2, both bursts were observed by MCAL but the GRID detector never observed the source at T_0 . In Figure 2, top left panel, is shown the *AGILE* exposure at $T_0 - 100$ s (the best available exposure for this radio burst), and in the top right panel the exposure at T_0 . For the second radio burst of Source 2 in the bottom left panel of Figure 2 is shown the exposure at T_0 and in the bottom right panel the best available exposure at $T_0 + 100$ s. Based on GRID exposures at the T_0 's, we focus our subsequent analysis to the bursts F and G of Source 1, and to both bursts (A and B) of Source 2. For all *AGILE* detectors the instruments response depends on the incident angle with respect to the pointing axis as described in e.g., Tavani et al. (2009, 2016).

3.1. MCAL fluence upper limits

The *AGILE*/MCAL is a detector that operates with seven different trigger windows, from the submillisecond ($\sim 300 \mu\text{s}$) timescale to a ~ 8 s timescale. We searched for impulsive triggered events in the MCAL data for time intervals centered at the FRB event times T_0 provided in Table 1. Details about the onboard trigger logic and data acquisition are given in the Appendix.

In Table 1 we show that 70% of Source 1 bursts and 100% of Source 2 bursts are inside the FoV of MCAL. Source 1 burst A is occulted by the Earth and there are no available data at the Source 1 burst B occurrence. No triggers were registered around T_0 's and no transients were thus recorded by MCAL. If MCAL is not

Table 1. Repeating FRBs and *AGILE* observations

FRB Radio Parameters				Event in the <i>AGILE</i> FoV		
Label	Day (yymmdd)	Arrival Time (UTC @ 400MHz)	Fluence (Jy ms)	MCAL	GRID	Super-A
Source 1: FRB 180916.J0158+65						
A	180916	10:15:19.8021	2.3	NO	NO	NO
B	181019	08:13:22.7507	2.7	-	-	-
C	181104	06:57:18.58524	2.5	YES	NO	NO
D	181104	07:07:01.591	2.0	YES	NO	NO
E	181120	05:56:06.23243	1.8	YES	NO	NO
F	181222	03:59:23.2082	27	YES	YES	NO
G	181223	03:51:28.96040	8.1	YES	YES	NO
H	181225	03:53:03.9260	1.9	YES	NO	NO
I	181226	03:43:30.1074	3.8	YES	NO	NO
L	190126	01:32:45.3289	2.0	-	-	-
Source 2: FRB 181030.J1054+73						
A	181030	04:13:13.0255	7.3	YES	NO	NO
B	181030	04:16:21.6546	2.2	YES	NO	NO

Note:

No *AGILE* data are available for 181019 and 190126. FRB parameters from C19.

triggered, ULs for the fluence can be obtained by evaluating the minimum detectable flux as a function of angle (based on the detector response matrix) as required by the onboard trigger logic at different timescales. MCAL therefore provides fluence ULs for the seven different timescales of the onboard trigger logic, for events that did not trigger the detector. As an example, in Figure 3 are reported the fluence ULs obtained by MCAL for the radio burst F of Source 1. Similar values are obtained also for burst G of Source 1 and for those of Source 2. The MeV-fluence ULs obtained for submillisecond and millisecond timescales (being of the order 10^{-8} erg cm $^{-2}$) are particularly important, as we discuss below.

3.2. GRID observations of Source 1 (FRB 180916.J0158+65)

As reported in Table 1, GRID has exposure of burst F and G of Source 1 at T_0 . The radio burst positions are inside the GRID FoV as shown in the right panels of Figure 1.

There is no known γ -ray source within a circle of radius 10 degrees, the usual *AGILE* Maximum Likelihood region of interest, at the position of the FRB. Since *AGILE* rotates every ~ 7 minutes around a direction pointing at the Sun, the GRID obtained exposures of the source for each satellite revolution not affected by Earth occultation and/or SAA passages. We consider two types of analysis (as in Verrecchia et al. 2017): (1) the "GRB detection mode" for short integration times (see Giuliani et al. 2010) within the interval $[0, +1000]$

(times refer to T_0) from 10 to 1000 s integration times, in the 50 MeV – 10 GeV band; (2) the *AGILE* Maximum Likelihood analysis (Bulgarelli et al. 2012) for long integration times, ranging from 1 day to 100 days, in the 100 MeV – 10 GeV band.

The short exposures of Source 1, with 10, 100 and 1000 s integration times during the first passage on its position, allowed us to obtain the 3σ flux ULs in the 50 MeV – 10 GeV band reported in Table 2; they range from 1.7×10^{-6} erg cm $^{-2}$ s $^{-1}$ to 1.5×10^{-8} erg cm $^{-2}$ s $^{-1}$. The UL values of bursts F and G are compatible, with the exception of $UL_{10s}^{1,F}$ that is ~ 4 times smaller with respect to $UL_{10s}^{1,G}$: this is because at T_0 the source was at the edge of the GRID FoV which is moving away from the source region. Its effective exposure is lower than in the same interval for Burst F.

The long exposures (with integrations of 1, 10 and 100 days) lead to the 3σ flux ULs (see Table 2) in the 100 MeV – 10 GeV band ranging from 4.1×10^{-10} erg cm $^{-2}$ s $^{-1}$ to 3.9×10^{-11} erg cm $^{-2}$ s $^{-1}$. In Figure 4, we show our γ -ray ULs for Source 1 burst F that we obtained for time intervals before and after the event. The short timescale values depend on the specific exposure and pointing geometry of the *AGILE* satellite.

3.3. GRID observations of Source 2 (FRB 181030.J1054+73)

None of the two bursts of Source 2 are inside *AGILE*/GRID FoV at T_0 , as shown in the top right panel and the bottom left panel of Figure 2. Also in this case, we split the analysis in short and long timescales, us-

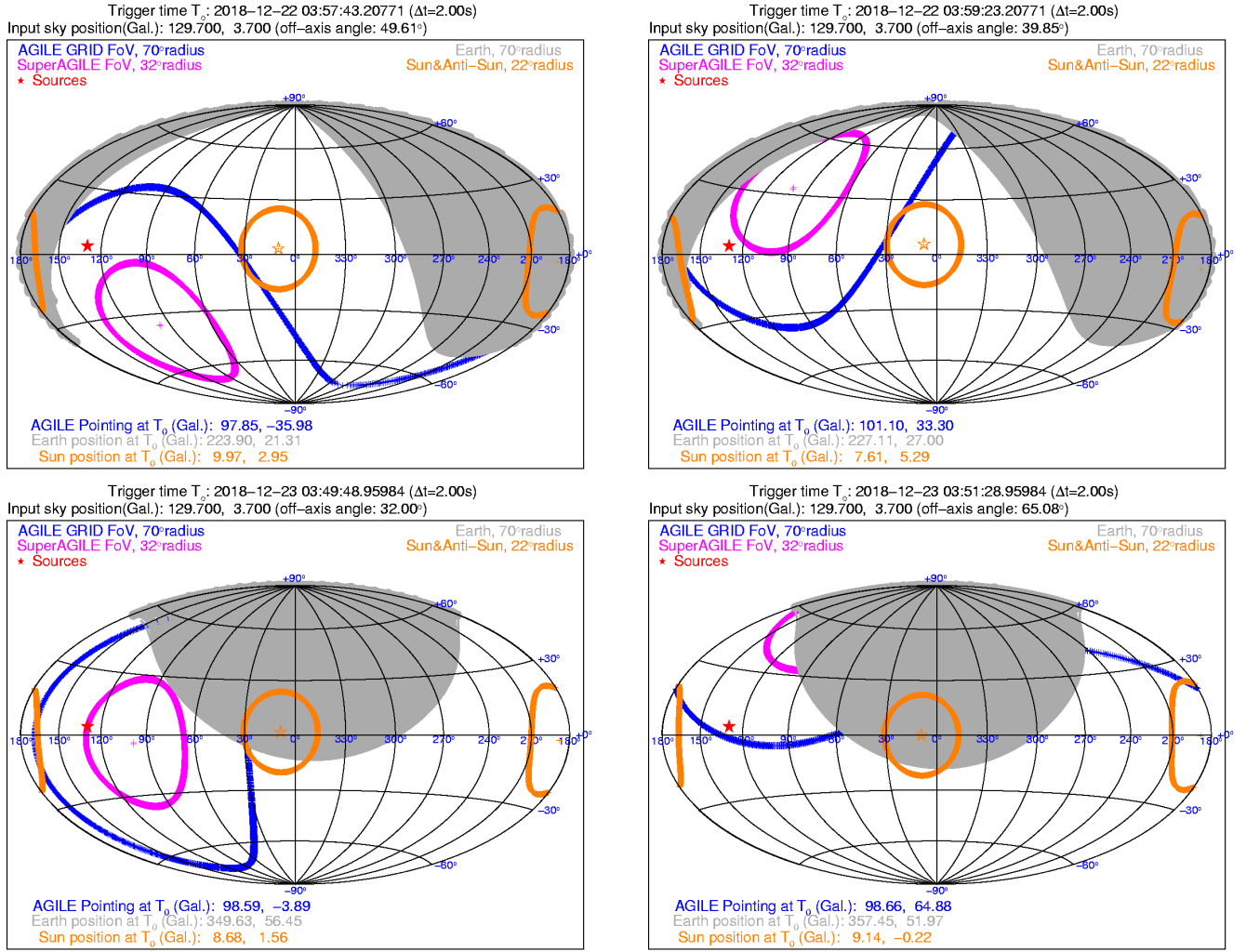


Figure 1. (Top panels:) *AGILE* exposure of burst F of Source 1 (FRB 180916.J0158+65) at $T_0^{1,F} - 100$ s (left panel) and at $T_0^{1,F}$ (right panel). Plots in Galactic coordinates. The position of the FRB is marked by a red star. The boundaries of the *AGILE*/GRID and Super-A FoVs are marked in blue and magenta color, respectively. (Bottom panels:) *AGILE* exposure of burst G of Source 1 at $T_0^{1,G} - 100$ s (left panel) and at $T_0^{1,G}$ (right panel). All images are ordered in time from left to right.

Table 2. *AGILE*/GRID flux ULs for the radio burst F, G of Source 1 and burst A of Source 2, as a function of integration timescales.

Name	$T_0 + 10^1$ s ^(a)	$T_0 + 10^2$ s ^(a)	$T_0 + 10^3$ s ^(a)	$T_0 + 10^0$ d ^(a)	$T_0 + 10^1$ d ^(a)	$T_0 + 10^2$ d ^(a)
Source 1-F	4.0×10^{-7}	3.6×10^{-8}	1.5×10^{-8}	4.1×10^{-10}	1.1×10^{-10}	3.9×10^{-11}
Source 1-G	1.7×10^{-6}	3.4×10^{-8}	1.6×10^{-8}	4.1×10^{-10}	1.1×10^{-10}	4.0×10^{-11}
Source 2-A	2.7×10^{-7} ^(b)	4.7×10^{-8} ^(b)	1.0×10^{-8}	7.3×10^{-10}	5.3×10^{-11}	1.8×10^{-11}

Notes:

(a): 3σ flux ULs ($\text{erg cm}^{-2} \text{s}^{-1}$) obtained for emission in the range 50 MeV – 10 GeV for the short integration timescales and 100 MeV – 10 GeV for the long ones, at each source positions.

(b): The first two ULs of Source 2 are evaluated on intervals [+390, +400] s and [+390, +490] s, respectively. These two intervals start as the source enters the exposed region during the *AGILE* spinning revolution.

ing the same integration times as in the previous case.

Furthermore, due to the small amount of time between

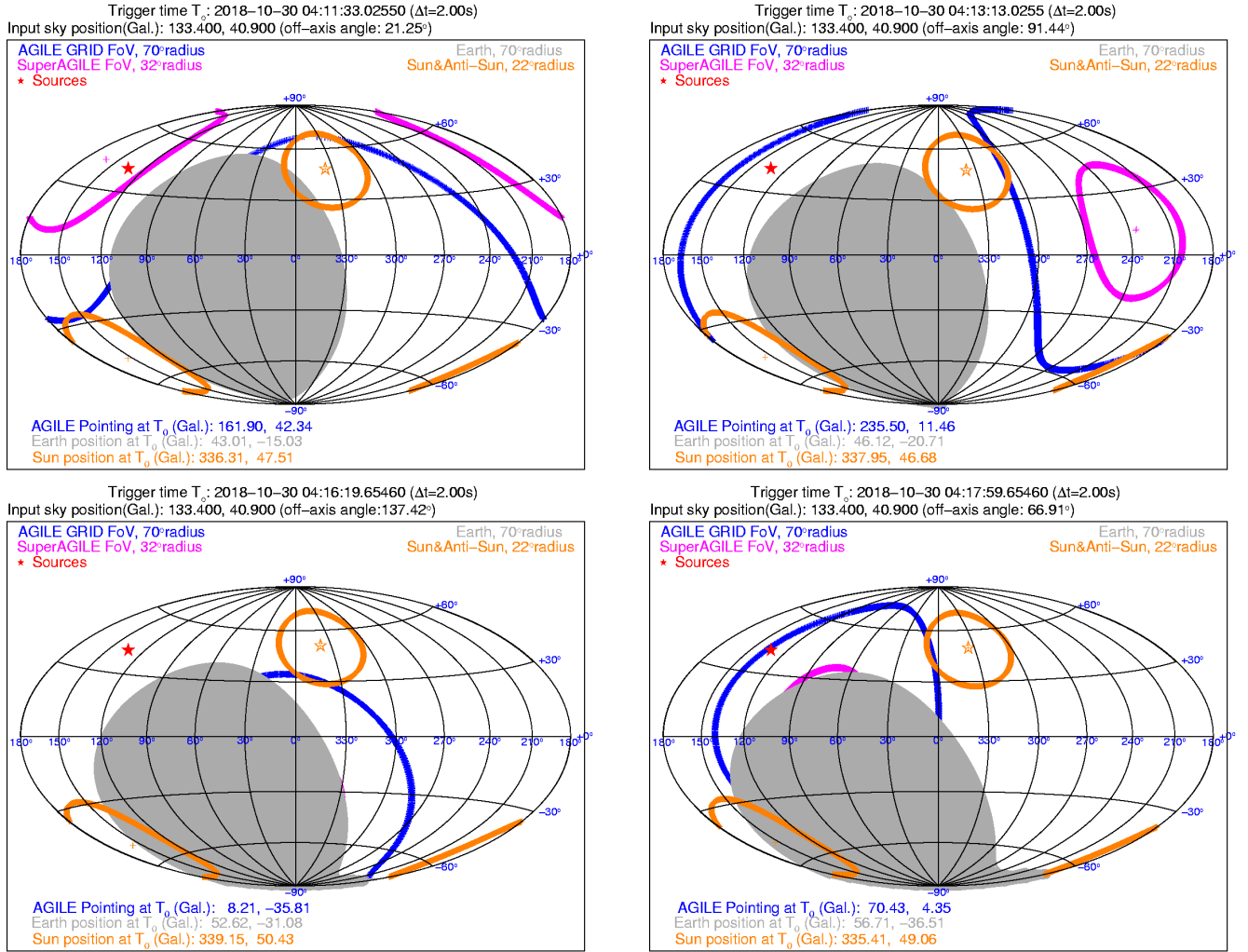


Figure 2. (Top panels:) *AGILE* exposure of burst A of Source 2 (FRB 181030.J1054+73) at $T_0^{2,A} - 100$ s (left panel) and at $T_0^{2,A}$ (right panel). Plots in Galactic coordinates. The position of the FRB is marked by a red star. The boundaries of the *AGILE*/GRID and Super-A FoVs are marked in blue and magenta color, respectively. (Bottom panels:) *AGILE* exposure of burst B of Source 2 at $T_0^{2,B}$ (left panel) and at $T_0^{2,B} + 100$ s (right panel). All images are ordered in time from left to right.

the two bursts (\sim few minutes), we made the analysis considering only the first repetition. The short exposures allowed us for this source to obtain the 3σ flux ULs in the 50 MeV – 10 GeV band (reported in Table 2), ranging from 2.7×10^{-7} erg cm $^{-2}$ s $^{-1}$ to 1.0×10^{-8} erg cm $^{-2}$ s $^{-1}$. The 10 and 100 s integration ULs were evaluated on intervals [+390, +400] s and [+390, +490] s, respectively, when the source entered the GRID FoV. For longer exposures we obtain ULs ranging from 7.3×10^{-10} erg cm $^{-2}$ s $^{-1}$ to 1.8×10^{-11} erg cm $^{-2}$ s $^{-1}$, in the 100 MeV – 10 GeV energy band (see Table 2).

4. DISCUSSION

The energy of the FRB radio burst emission is believed to be a small fraction of the total energy involved in any plasma configuration capable of radiating isotropically-estimated energies of 10^{39} erg or larger for FRBs with large DMs (e.g., Cordes & Chatterjee 2019). If the large-DM FRBs are indeed at extragalactic distances, the underlying energy sources are most likely associated with phenomena involving compact objects, either neutron stars or black holes in peculiar states of emission. Therefore, constraining the energetics of the underlying plasma source for small-DM FRBs offers a unique way of exploring energy and luminosity ranges that are substantially smaller than those applicable to large-DM/extragalactic FRBs. Observed quan-

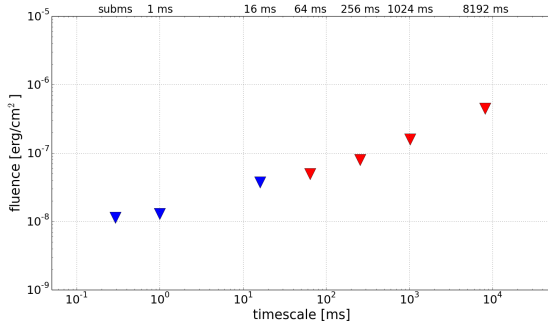


Figure 3. *AGILE/MCAL* fluence ULs in the energy range 0.4–100 MeV for the F radio burst of Source 1 as a function of integration timescales. Similar values are obtained for the burst G. Blue markers show the hardware trigger logic ULs, while red markers show the software trigger logic ones (see the Appendix for details).

tities depend on unknown beaming. In the following we assume isotropic emission for our estimates of energies and luminosities. Our reference fluence F' in the millisecond range is the typical *AGILE/MCAL* fluence UL obtained for several events of Table 1, that is $F'_{MeV} = 10^{-8} \text{ erg cm}^{-2}$.

Let us consider first the extragalactic distance hypothesis for both Source 1 and Source 2. We assume here the distance $d = 150 \text{ Mpc}$ for both Source 1 and Source 2, in agreement with the recent detection of Source 1 by Marcote et al. (2020). Our value of F' translates into an UL for the radiated energy into the MeV range, $E_{MeV,UL} = 4\pi F' d_{150M}^2 \simeq (2.2 \times 10^{46} \text{ erg}) d_{150M}^2$, where $d_{150M} = d/150 \text{ Mpc}$ with d the source distance from Earth. This value of $E_{MeV,UL}$ should be compared with the energy involved in the radio burst observation, $E_{radio,iso} \simeq (2.7 \times 10^{37} \text{ erg}) S_{\nu,Jy} \delta t_{ms} \Delta\nu_{GHz} d_{150M}^2$, where the measured FRB flux density in the radio band is $S_{\nu,Jy}$ in units of jansky, δt_{ms} is the temporal width in units of milliseconds, and $\Delta\nu_{GHz}$ is the radio bandwidth in units of GHz. Note that events F and G of Source 1 have $S_{\nu,Jy} \sim 10$. If the two energies are compared for a time interval (e.g., milliseconds) assumed to be the same for the radio and MeV emissions, the ratio $E_{radio,iso}/E_{MeV,UL} \gtrsim 10^{-8}$ clearly indicates the marginal contribution of the radio emission from the point of view of the overall energetics for events that are expected to be detected in the MeV range. *MCAL* UL's for 1–10 s integrations are larger by more than one order of magnitude compared with that of millisecond timescales (see Figure 3), and the corresponding UL on the involved energy is $E_{MeV,UL} \simeq (\text{a few } 10^{47} \text{ erg}) d_{150M}^2$.

If Source 2 is located within our Galaxy or Galactic halo, our results are more constraining. In this case,

our value of F' translates into the UL, $E_{MeV,UL} = 4\pi F' d_{100k}^2 \simeq (10^{40} \text{ erg}) d_{100k}^2$, where $d_{100k} = d/100 \text{ kpc}$, and the energy involved in the radio burst is $E_{radio,iso} \simeq (1.2 \times 10^{31} \text{ erg}) S_{\nu,Jy} \delta t_{ms} \Delta\nu_{GHz} d_{100k}^2$.

MeV-radiated energies of order of $10^{40} - 10^{41} \text{ erg}$ are relevant for systems hosting a magnetar-like star, that is for compact objects whose outbursts are energized by either magnetic instabilities or by magnetospheric acceleration phenomena. The very large magnetic fields associated with magnetars (of the order of $B_m \sim 10^{14} - 10^{16} \text{ G}$) in principle can be associated with maximal energies $E_m \sim R_m^3 B_m^2 / 6 \simeq (2 \times 10^{49} \text{ erg}) B_{m,16}^2$, with $B_{m,16}$ the magnetar inner magnetic field in units of 10^{16} G and where we assumed a magnetar radius $R_m = 10^6 \text{ cm}$. It is not clear how and when fractions of the total magnetic energy can be dissipated by special instabilities. The analysis of Thompson & Duncan 1996 implies a timescale of $\tau_a \sim 10^{11} \text{ s}$ for ambipolar diffusion of the inner magnetar field, and therefore an average luminosity

$$L_a \sim E_m / \tau_a \sim (10^{38} \text{ erg s}^{-1}) E_{m,49} \tau_{a,11}^{-1} \quad (1)$$

where $E_{m,49}$ is the maximal energy in units of 10^{49} erg , and $\tau_{a,11}$ is the diffusion time in units of 10^{11} s . Smaller values of τ_a (e.g. Beloborodov 2017) and/or of $B_{m,16}^2$ imply larger/smaller average luminosities. We consider the luminosity L_a of Eq. 1 as a reasonable reference for comparison with our observations.

AGILE short time observations summarized in Table 1 and Figs. 1–3 constrain any flaring activity of a putative magnetar associated with Source 2 and subject to sudden instabilities. Any MeV-radiated energy associated with simultaneous FRB activity is constrained to be less than $E_{MeV,UL} \sim (10^{40} - 10^{41} \text{ erg}) d_{100k}^2$. Note that the former value applies for timescales of milliseconds or less, and the latter value to timescales near 200 ms. When compared with the 2004 powerful flare of SGR 1806–20 that radiated $E_{MeV,SGR} \simeq 2 \times 10^{46} \text{ erg}$ within $\sim 200 \text{ ms}$ in the MeV range (Palmer et al. 2005; Hurley et al. 2005) our observations clearly exclude such an occurrence. If we use the observed peak energy of 10^{46} erg in obtaining the fraction ξ of available magnetic energy being radiated into the MeV range, we deduce $\xi \sim E_{MeV,SGR}/E_m \sim 10^{-3} B_{16}^{-2}$. We therefore obtain the ULs of the flaring energies associable with the repeating FRBs of Table 1, $E_* \sim E_{MeV,UL}/\xi \sim (10^{43} - 10^{44} \text{ erg}) B_{16}^{-2} d_{100k}^2$. These values exclude major magnetic flaring activity from magnetars with inner magnetic fields near 10^{16} G . Therefore, either the magnetic field of the associated magnetar is smaller than 10^{16} G , or the intensities of the MeV flares that we are trying to detect are substantially smaller than those ob-

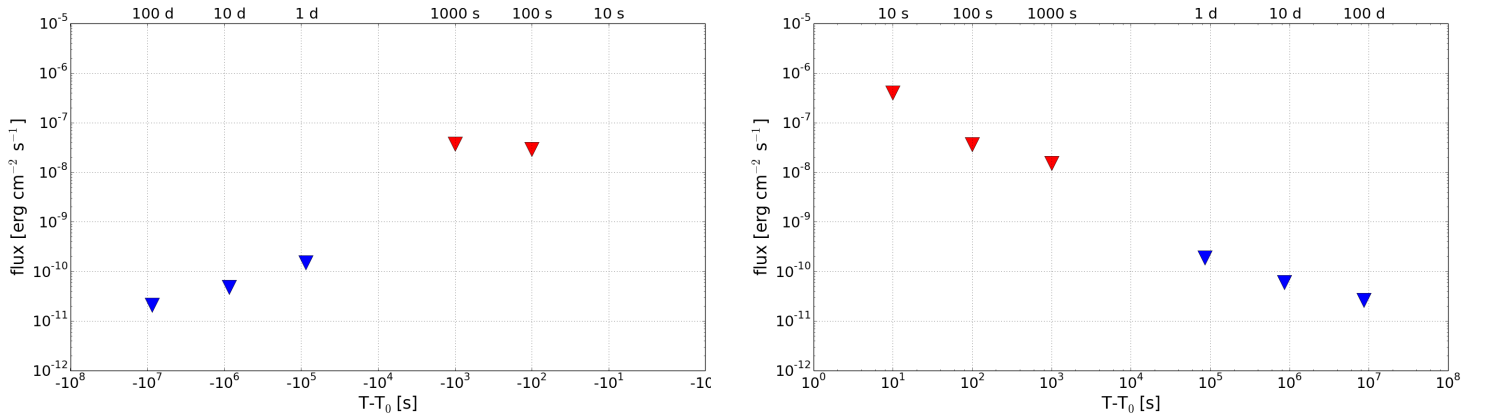


Figure 4. *AGILE*/GRID 2σ flux ULs for the F burst of Source 1 as a function of integration times pre- and post-burst T_0 . The symbols mark the beginning (left panel) or the ending (right panel) of the integration time intervals that have FRB T_0 as one extreme time value. The short timescale values depend on the specific exposure and pointing geometry of the *AGILE* satellite. The energy ranges are $50 \text{ MeV} < E < 10 \text{ GeV}$ for timescales $10, 10^2, 10^3 \text{ s}$ (red markers), and $100 \text{ MeV} < E < 10 \text{ GeV}$ for longer integrations (blue markers).

served in the case of the giant flare of SGR 1806-20. Both of these possibilities are reasonable, and we consider these constraints an interesting outcome of our observations.

Additional constraints derive from *AGILE* gamma-ray observations of Source 1 and Source 2 with long time integrations. *AGILE*/GRID measurements at the locations of the repeating FRBs of Table 1 constrain possible high-energy emission above 50 MeV on intermediate and long timescales as summarized in Table 2. If we consider the long timescale flux ULs for 100 day integrations, we obtain $F_\gamma \sim (2-4) \times 10^{-11} \text{ erg cm}^{-2} \text{ s}^{-1}$. Therefore, for the 150 Mpc distance of Source 1 we obtain an UL on the isotropic luminosity emitted above 50 MeV, $L_{\gamma,UL} \simeq (5-10) \times 10^{43} d_{150\text{Mpc}}^2 \text{ erg s}^{-1}$. For an assumed distance within our Galactic halo of Source 2, we obtain

$$L_{\gamma,UL} \simeq 2 \times 10^{37} d_{100\text{k}}^2 \text{ erg s}^{-1}. \quad (2)$$

This luminosity should be compared with that of Eq. 1. A comparison of these two luminosities of the same order of magnitude suggests a not very constraining UL on the 50 MeV-efficiency $\xi_{GeV} \lesssim 0.2$. On the other hand, ULs of the type of Eq. 2 are the lowest ever obtained in the γ -ray energy range for a possibly FRB nearby source, and constrain the flaring activity of the underlying object of Source 2 (that may turn out to be closer than Source 1 based on its excess DM).

5. CONCLUSIONS

Fast radio bursts continue to be puzzling with features that are not satisfactorily explained in current modelling

of compact objects. A crucial diagnostic of the physical processes involved in FRBs is provided by X-ray and γ -ray simultaneous observations. In this paper we focused on two distinct FRB sources that erratically repeat and that have low intrinsic DM indicating relatively small distances. From the hypothesis that the excess DM is directly related to distances, these two FRBs can be considered among the closest ever detected in the radio band. They are therefore the most interesting for constraining their high energy emission. The recent detection of Source 1 associated with a nearby spiral galaxy at 150 Mpc distance (Marcote et al. 2020) adds weight to this prospect. It is interesting to note that if also Source 2 is located outside our Galaxy, a UL on its distance is of the order of 100 Mpc (as noticed by C19).

AGILE observations provide important constraints on the prompt (millisecond and hundreds of millisecond timescales) emission in the sub-MeV/MeV range, and exclude strong magnetar flares of the type of the 2004 event from SGR 1806-20. This is especially true for a Source 2 Galactic halo distance, but applies also to distances of the order of 100 Mpc. Our UL of the MeV isotropic emitted energy at millisecond/hundreds of millisecond timescales $E_{\text{MeV},UL} \sim (10^{40} - 10^{41} \text{ erg}) d_{100\text{k}}^2$ constrains magnetar models for Source 2. For larger distances, our energy UL is less compelling, but in any case reaches values of the order of the emitted MeV energy from the giant 2004 outburst of SGR 1806-20 during its first few hundreds milliseconds of emission. Indeed, we note that the maximum distance out of which we can exclude such a large flare from FRB sources is of the order of 100 Mpc.

Furthermore, we constrain the persistent long timescale γ -ray emission above 30 MeV from the repeating FRBs of Table 1. For locations up to 150 Mpc, our ULs constrain the γ -ray emitted power to be smaller than $L_{\gamma,UL} \simeq 5 \times 10^{43} \text{ d}_{150\text{M}}^2 \text{ erg s}^{-1}$, i.e., substantially smaller than those detected by nearby blazars. If the Source 2 location is within our Galactic halo, our UL of the average isotropic γ -ray luminosity, $L_{\gamma,UL} \simeq 2 \times 10^{37} \text{ d}_{100\text{k}}^2 \text{ erg s}^{-1}$, excludes steady magnetar-like power to γ -ray conversions of the order of 10% for the source in the Galactic halo.

In conclusion, *AGILE* observations constrain the activity of the underlying energy source both on short and long timescales. Major flaring activities of the type of SGR 1806-20 are clearly excluded for a Source 2 within our Galactic halo, with the *AGILE* MeV fluence ULs reaching values nearly 3 orders of magnitude less than the SGR 1806-20 flare for a nearby source. The γ -ray limits on the isotropic luminosity obtained above 30 MeV are somewhat less constraining. In any case, one

can exclude the presence of an energy source at levels reported for different timescales in Table 2.

FRBs continue to be sources of great interest. More observations are needed to further constrain the emission process and the physical properties associated with the detected radio bursts. Having determined the distance of Source 1 is of great relevance. Establishing the distance of Source 2 (which has the smallest excess DM ever measured) would also be invaluable in constraining models. *AGILE* continues its observations of the γ -ray sky, and will provide useful data for the search of FRB high-energy counterparts.

Acknowledgments: We acknowledge comments by two anonymous referees that were taken into account and contributed in improving our revised manuscript. The investigation was carried out with partial support by the ASI grant no. I/028/12/05.

APPENDIX

As implemented in other contexts of searches for MCAL transients at specific times provided by external information (e.g., gravitational wave events), we searched for MCAL triggers in 100 s time windows centered at the T_0 .

The MCAL burst search logic is based on the criterion that a transient event releases a number of counts above a given threshold over the background. The background count rate depends on the specific timescale and energy range and it is therefore evaluated by adopting different rate meters (RMs): such RMs are characterized by different search integration time (SIT) windows (Hardware trigger logic working on timescales of: 0.293, 1, and 16 ms; Software trigger logic working on timescales of: 64, 256, 1024, and 8192 ms), and covering three energy ranges (low energy: 0.3–1.4 MeV; medium energy: 1.4–3 MeV; high energy: 3–100 MeV).

In particular, the hardware 0.293 ms (or “sub-ms”) search window is a key feature of the *AGILE* MCAL. Such a feature is crucial for the detection of short-duration events, such as terrestrial gamma-ray flashes (TGFs), lasting few hundreds of microseconds (Marisaldi et al. 2010, 2014), as well as GRBs with exceptional high fluxes (e.g., GRB 180914B, Ursi et al. 2018).

MCAL triggered data acquisitions are issued whenever a given threshold count rate is exceeded. Such thresholds depend on the involved SIT duration. Shortest duration timescales (hardware logic) adopt a static trigger logic, which imposes a fixed threshold count rate S . For a typical MCAL background rate of 580 Hz, a signal should have at least the following significances in order to trigger one or more onboard hardware logics (as described in Ursi et al. 2019):

- Sub-ms: at least seven counts on a background of 580 Hz (~ 0.2 counts/300 μs), corresponding to $\sim 17\sigma$;
- 1 ms: at least eight counts on a background of 580 Hz (~ 0.6 counts/1 ms), corresponding $\sim 10\sigma$; and
- 16 ms: at least 23 counts on a background of 580 Hz (~ 9 counts/16 ms), corresponding at least at 4σ .

The corresponding false alarm rates (FARs) are $\sim 6 \times 10^{-4}$ Hz for the sub-ms, 3×10^{-4} Hz for the 1 ms, and 2×10^{-2} Hz for the 16 ms time scales. These MCAL trigger threshold values were selected mainly for the e.m. counterparts detection for the LV GW events during the O2 (2017) and O3 (2019–2020) observing runs. The main goal of this configuration was to increase the total onboard exposure time of the detector and also to enhance the sensitivity to short-duration impulsive events. This configuration increases the probability to have weak, short events falling within the triggered acquisition time windows (as for GW170104; see Verrecchia et al. 2017). As a consequence

in the case of a candidate coincidence, we are ready to evaluate the c.l. of signals occurring close in time to an external event according to the post-trial probability of the signal with respect to the external event time, as in [Connaughton et al. \(2016\)](#). This probability strongly depends on the FAR and on the time interval between the signal and the external event, apart from the signal intrinsic significance above the background.

On the other hand, software logic timescales adopt an adaptive trigger logic, which evaluates the background rate in the given timescale and estimate a related $S = B + N\sigma$ threshold count rate (with N number of standard deviations). Whenever one or more of these thresholds are exceeded, a Burst-START condition is issued and a data acquisition starts. The duration of the data acquisition depends on the Burst-STOP condition, which can be encountered when all RMs go back to a normal background level, or can be forced after a given amount of time (which depends on the timescale). Data are stored in a cyclic buffer, together with pre- and post-burst data streams, regarding time intervals occurring before and after the main burst acquisition. The MCAL trigger logic is flexible and all parameters are fully configurable on ground.

REFERENCES

- Barbiellini, G., Fedel, G., Liello, F., et al., 2002, NIMPA, 490, 146
- Beloborodov, A. M., 2017, ApJL, 843, L26
- Bulgarelli, A., Chen, A. W., Tavani, M., et al. 2012, A&A, 540, A79
- Bulgarelli, A., Trifoglio, M., & Gianotti, F., 2014, ApJ, 781, 19
- Champion, D. J., Petroff, E., Kramer, M., et al., 2016, MNRAS, 460, L30
- Chatterjee, S., Law, C. J., Wharton, R. S., et al., 2017, Nature, 541, 58
- The CHIME/FRB Collaboration, Amiri, M., Bandura, K., Bhardwaj, M., et al. 2019a, Nature, 566, 230
- The CHIME/FRB Collaboration, Amiri, M., Bandura, K., Bhardwaj, M., et al. 2019b, Nature, 566, 235
- The CHIME/FRB Collaboration, Andersen, B. C., Bandura, K., Bhardwaj, M., et al. 2019c, arXiv e-prints, arXiv:1908.03507 (C19)
- Connaughton, V., Burns, E., Goldstein, A., et al. 2016, ApJL, 826, L6
- Cordes, J. M., and Chatterjee, S., 2019, ARA&A, 119, 161101
- Cordes, J. M., & Lazio, T. J. W. 2002, arXiv preprint astro-ph/0207156
- Cunningham, V., Cenko, S. B., Burns, E., et al., 2019, ApJ, 879, 40
- Faucher-Giguère, C. A., & Kaspi, V. M., 2006, ApJ, 643, 332
- Feroci, M., Costa, E., Soffitta, P., et al., 2007, NIMPA, 581, 728
- Fuschino, F., Labanti, C., Galli, M., et al. 2008, NIMPA, 588, 17
- Giuliani, A., Fuschino, F., Vianello, G., et al. 2010, ApJL, 708, L84
- Hessels, J.W.T., Spitler, L. G., Seymour, A. D., et al., 2019, ApJ, 876L, 23
- Hurley, K., Boggs, S. E., Smith, D. M., et al., 2005, Nature, 434, 1098
- Labanti, C., Marisaldi, M., Fuschino, F., et al. 2009, NIMPA, 598, 470
- Lorimer, D. R., Faulkner, A. J., Lyne, A. G., et al., 2006, MNRAS, 372, 777
- Lorimer, D. R., Bailes, M., McLaughlin, M. A., Narkevic, D. J., & Crawford, F., 2007, Science, 318, 777
- Marcote, B., Paragi, Z., Hessels, J. W. T., et al., 2017, ApJL, 834, L8
- Marcote, B., Nimmo, K., Hessels, J. W. T., et al., 2020, Nature, 577, 190
- Marisaldi, M., Labanti, C., Fuschino, F., et al., 2008, A&A, 490, 1151
- Marisaldi, M., Labanti, C., Fuschino, F., et al., 2010, Journal of Geophysical Research (Space Physics), 115, 2156
- Marisaldi, M., Fuschino, F., Tavani, M., et al., 2014, Journal of Geophysical Research (Space Physics), 119, 1337
- Martone, R., Guidorzi, C., Margutti, R., Nicastro, L., Amati, L., et al., 2019, arXiv e-prints, arXiv:1909.07165
- Michilli, D., Seymour, A., Hessels, J. W. T., et al., 2018, Nature, 533, 132
- McQuinn, M., 2014, ApJL, 780, L33
- Metzger, B. D., Margalit, B., and Sironi, L., 2019a, MNRAS, 485, 4091
- Olausen, S. A., & Kaspi, V. M., 2014, ApJS, 212, 6
- Petroff, E., Barr, E. D., Jameson, A., et al., 2016, PASA, 33, e045
- Palmer, D. M., Barthelmy, S., Gehrels, N., et al., 2005, Nature, 434, 1107
- Pittori, C., 2013, NuPhS, 239, 104
- Prochaska, J. X., & Zheng, Y., 2019, MNRAS, 485, 648
- Scholz, P., Bogdanov, S., Hessels, J. W. T., et al., 2017, ApJ, 846, 80
- Spitler, L. G., Scholz, P., Hessels, J. W. T., et al., 2016, Nature, 531, 202
- Tavani, M., Barbiellini, G., Argan, A., et al., 2009, A&A, 502, 995
- Tavani, M., Marisaldi, M., Labanti, C., et al., 2011, Physical Review Letters, 106, 018501
- Tavani, M., Pittori, C., Verrecchia, F., et al. 2016, ApJL, 825, L4
- Thompson, C. & Duncan, R. C., 1996, ApJ, 473, 322
- Ursi, A., Tavani, M., Verrecchia, F., et al., 2019, ApJ, 871, 27
- Ursi, A., Tavani, M., Argan, A., et al., 2018, GCN, 23226, 1
- Verrecchia, F., Tavani, M., Donnarumma, I., et al., 2017, ApJL, 850, L27
- Verrecchia, F., Tavani, M., Bulgarelli, A., et al., 2019, RLSFN, 30, 71, doi:10.1007/s12210-019-00854-0
- Verrecchia, F., Tavani, M., Donnarumma, I., et al., 2018, IAUS, 338, 84
- Yao, J. M., Manchester, R.N., & Wang, N., 2017, ApJ, 835, 29